AGU PUBLICATIONS

JGR

Journal of Geophysical Research: Solid Earth

RESEARCH ARTICLE
10.1002/2017JB015130

Key Points:
- Pore fluid overpressure may develop in low-permeability fault gouges during shear-enhanced compaction
- The mechanical effect of pore fluid overpressures is characterized in experiments and modeled numerically
- Compaction weakening is important to consider in experiments and may have a first-order influence on the mechanical behavior of faults in nature

Correspondence to:
D. R. Faulkner,
faulkner@liv.ac.uk

Citation:
Faulkner, D. R., Sanchez-Roa, C., Boulton, C., & den Hartog, S. A. M. (2018). Pore fluid pressure development in compacting fault gouge in theory, experiments, and nature. *Journal of Geophysical Research: Solid Earth*, *123*, 226–241. https://doi.org/10.1002/2017JB015130

Received 19 OCT 2017
Accepted 21 DEC 2017
Accepted article online 28 DEC 2017
Published online 18 JAN 2018

Pore Fluid Pressure Development in Compacting Fault Gouge in Theory, Experiments, and Nature

D. R. Faulkner[1], C. Sanchez-Roa[2], C. Boulton[1,3], and S. A. M. den Hartog[1]

[1]Rock Deformation Laboratory, Department of Earth, Ocean and Ecological Sciences, University of Liverpool, Liverpool, UK, [2]Departamento de Geología y CEACTierra, Unidad Asociada IACT (CSIC-UGR), Universidad de Jaén, Jaén, Spain, [3]Now at School of Geography, Environment, and Earth Sciences, Victoria University of Wellington, Wellington, New Zealand

Abstract The strength of fault zones is strongly dependent on pore fluid pressures within them. Moreover, transient changes in pore fluid pressure can lead to a variety of slip behavior from creep to unstable slip manifested as earthquakes or slow slip events. The frictional properties of low-permeability fault gouge in nature and experiment can be affected by pore fluid pressure development through compaction within the gouge layer, even when the boundaries are drained. Here the conditions under which significant pore fluid pressures develop are analyzed analytically, numerically, and experimentally. Friction experiments on low-permeability fault gouge at different sliding velocities show progressive weakening as slip rate is increased, indicating that faster experiments are incapable of draining the pore fluid pressure produced by compaction. Experiments are used to constrain the evolution of the permeability and pore volume needed for numerical modeling of pore fluid pressure build up. The numerical results are in good agreement with the experiments, indicating that the principal physical processes have been considered. The model is used to analyze the effect of pore fluid pressure transients on the determination of the frictional properties, illustrating that intrinsic velocity-strengthening behavior can appear velocity weakening if pore fluid pressure is not given sufficient time to equilibrate. The results illustrate that care must be taken when measuring experimentally the frictional characteristics of low-permeability fault gouge. The contribution of compaction-induced pore fluid pressurization leading to weakening of natural faults is considered. Cyclic pressurization of pore fluid within fault gouge during successive earthquakes on larger faults may reset porosity and hence the capacity for compaction weakening.

1. Introduction

Variations in pore fluid pressure within faults profoundly affect their mechanical behavior. On long timescales, the maintenance of elevated pore pressure within faults can lead to long-term weakening by reducing effective normal stress acting on the fault, thereby lowering the shear stress on the fault required to promote sliding (Hubbert & Rubey, 1959). This process has been suggested as a candidate mechanism to explain long-term slip on misoriented "weak" faults such as the San Andreas Fault in California or low-angle normal faults (Byerlee, 1990; Collettini & Sibson, 2001; Faulkner & Rutter, 2001). On intermediate timescales, transient creep events on faults or slow earthquakes have been postulated to be related to high pore fluid pressure (Frank et al., 2015; Rubin, 2008). On shorter timescales, earthquake nucleation is often considered in terms of a rate and state friction framework (Dieterich, 1979; Ruina, 1983), where small changes in the friction coefficient due to variations in the slip velocity give rise to the onset of instability. Recent studies have started to consider the role of fluid pressure, as even small changes in pore fluid pressure from compaction, dilation, or thermal effects will produce first-order changes in the apparent friction coefficient via changes in the effective normal stress that may, or may not, promote instability and earthquake rupture (Bizzarri & Cocco, 2006; Garagash, 2012; Lockner & Byerlee, 1994; Noda & Lapusta, 2010; Samuelson et al., 2009; Segall & Rice, 1995).

Pore fluids can produce both mechanical and chemical effects. Only the mechanical effects are considered in this work. The influence of pore fluid pressure on the mechanics of faults depends on the ability of the fault zone to (a) produce pore fluid pressure transients and (b) to drain away excess pore fluid pressure. Time scales, length scales, and the intrinsic hydraulic properties (including permeability) of the fault zone become key factors. Timescales for diffusion of pore fluid pressures vary widely in natural faulting; long-term fault creep occurs on timescales of millions of years whereas earthquake rupture occurs on timescales of seconds. In terms of length scales, mature faults vary widely in their width, with high-strain cores varying from several

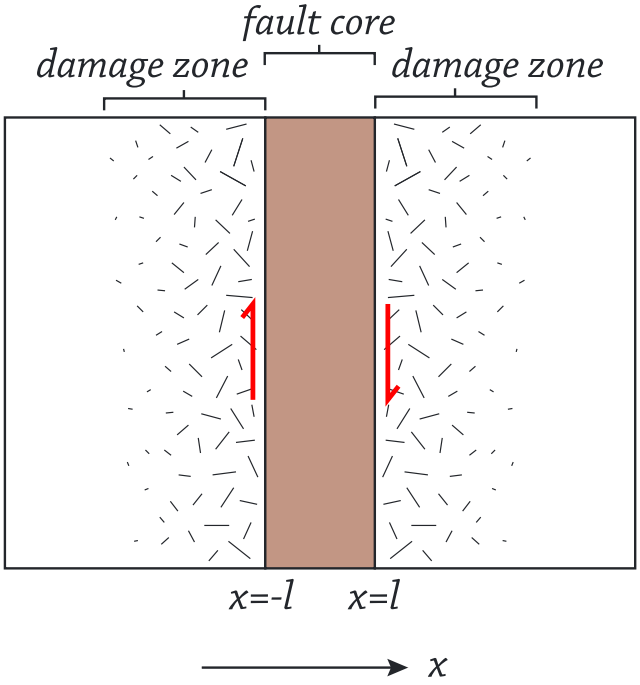

Figure 1. Schematic diagram that shows a gouge layer (fault core) embedded within a more porous and permeable damage zone. The damage zone provides a drained boundary at the limits of the fault core. The sketch also illustrates the model setup, with x in the direction perpendicular to the fault core, which stretches from $-l$ to l.

centimeters up to several meters (Chester et al., 1993; Faulkner et al., 2008). In terms of permeability, faults typically contain a core of very fine-grained fault gouge that is often clay rich. These characteristics give rise to very low permeability (Behnsen & Faulkner, 2011; Faulkner & Rutter, 1998; Ikari et al., 2009; Morrow et al., 1981; Wibberley & Shimamoto, 2003). Damage zones of faults that surround the high-strain fault core are much more permeable than low-porosity protoliths because of fracture damage (Chester & Logan, 1986; Mitchell & Faulkner, 2008, 2012). Hence, the permeability and length scale of the fault core determine the development of pore fluid overpressures since fluid is likely to be efficiently drained once it reaches the boundary between the fault core and damage zone.

It is important to understand how pore fluid pressure develops not only in nature but also in laboratory experiments, where the overall strength and constitutive parameters of natural and analogue fault zone materials are determined and used to model natural systems. If the development of pore fluid pressure within experimental fault gouges is not understood or considered, then a nominally "controlled" experiment, where the pore fluid pressure is maintained at the boundaries of the sheared layer, may give misleading data for the bulk frictional strength. Undrained or partially drained conditions can develop within experimental samples, yielding internal pore fluid pressures that differ from those along measured and controlled boundaries (Ikari et al., 2009; Morrow et al., 2017; Sleep & Blanpied, 1992). Moreover, experiments designed to determine the rate and state constitutive parameters (Dieterich, 1979; Ruina, 1983), where load-point velocity steps are introduced, may be subject to variations in pore pressure that can overwhelm the material's intrinsic frictional response and give erroneous values for the rate and state friction parameters.

There is a clear need to develop a better physical understanding of what affects the mechanical properties of fault gouges. By developing a physical understanding of the constitutive behavior of experimental faults, results may be extrapolated to faults under conditions applicable to those in the Earth, including high pressures and temperatures and strain rates that vary from mm/yr to m/s. This paper aims to contribute to this goal by identifying and quantifying the effect of pore fluid pressurization from compaction on the frictional properties of low-permeability fault gouges. This is particularly important as often these pore pressure transients cannot be measured in experiments as they occur locally within the fault gouge even when the boundaries are drained, leading to "apparent" frictional strength, based on the assumption that the pore fluid pressure is the same in the shearing layer as that maintained at the boundaries. The influence of compaction on the overall bulk strength and on the rate and state frictional parameters derived from velocity-stepping tests is also considered.

In this work, the theory of pore fluid pressure buildup from compaction is developed; then, results from new experiments on a natural fault gouge recovered during the Alpine Fault drilling project are presented to provide constraints for numerical modeling. Numerical models are subsequently used to illustrate the transient effects of pore fluid pressurization from compaction produced from shearing (shear-enhanced compaction, hereafter largely referred to as compaction) on the strength evolution. Finally, the implications of the analysis for natural faulting are discussed.

2. Fluid Pressure Buildup From Compaction During Loading and Shear in Low-Permeability Fault Gouges: Solution With Constant κ and A

There is ample evidence for shear-enhanced compaction of fault gouge in the laboratory (e.g., Crawford et al., 2008; Marone et al., 1990). As compaction proceeds, the pore fluid may become pressurized, depending on the rate of compaction and the hydraulic diffusivity of the gouge layer. The general scheme and model setup is illustrated in Figure 1.

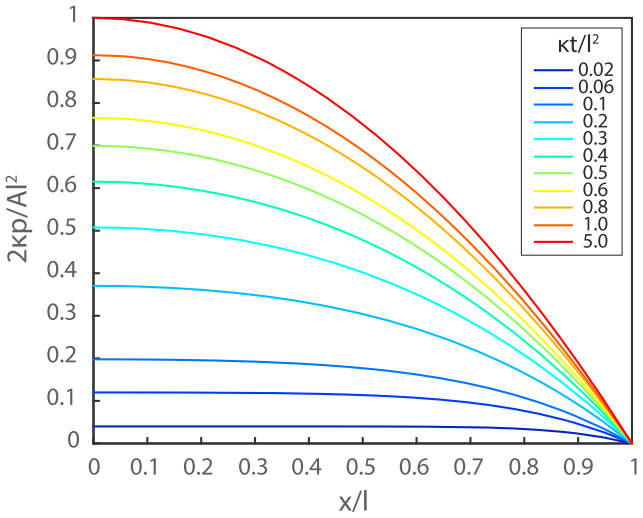

Figure 2. The buildup of normalized pore fluid pressure plotted against distance across a half layer with time. All the parameters are dimensionless. The pore fluid pressure increases uniformly within the layer with time (indicated by different colors) but is maintained at zero, or at the initial pore fluid pressure p_0, at the boundaries. The system eventually reaches a steady state, where fluid pressure diffusion to the boundaries balances the generation of fluid pressure in the layer.

The pore fluid pressure changes within a fault gouge layer during compaction can be described using the one dimensional diffusion equation with a source term, a rate of pore fluid pressure increase per unit time t, for a layer bounded by two parallel planes (Carslaw & Jaeger, 1959)

$$\frac{\partial p}{\partial t} = \kappa \frac{\partial^2 p}{\partial x^2} + A \qquad -l \le x \le l, \qquad t \ge 0 \tag{1}$$

where p = pore fluid pressure (Pa), x = perpendicular distance across the gouge layer (m), κ = hydraulic diffusivity (m^2/s), and A = source term (Pa/s) with simple boundary conditions $p(-l, t) = p_0$, $p(l, t) = p_0$, $p(x, 0) = p_0$, and where

$$\kappa = \frac{k}{\beta_c \eta} \tag{2}$$

k = permeability (m^2), β_c = storage capacity (Pa^{-1}), and η = fluid viscosity (Pa s). The p_0 is a constant pressure maintained at the boundaries of the layer.

In laboratory experiments, a constant pore fluid pressure is often servo-controlled at the boundaries of the fault gouge layer satisfying the boundary conditions for equation (1). If both the pore pressure production rate (source term A) and the hydraulic diffusivity κ are constants, then analytical solutions for equation (1) exist. Carslaw and Jaeger (1959) determined the solution for this problem as a function of distance x across a layer of thickness 2 l and time t. The p_0 here is zero. Their solution has been recast from temperature to pressure p:

$$p_{(x,t)} = \frac{Al^2}{2\kappa}\left(1 - \frac{x^2}{l^2} - \frac{32}{\pi^2}\sum_{n=0}^{\infty}\frac{(-1)^n}{(2n+1)^3}\cos\frac{(2n+1)\pi x}{2l}\exp\left[\frac{-\kappa(2n+1)^2\pi^2 t}{4l^2}\right]\right) \tag{3}$$

The analytical solution (equation (3)) can be used to illustrate the buildup of pore pressure with time with a constant pore pressure production rate A (Figure 2). The analytical solution here includes the sum of an infinite series. However, the summation terms quickly become negligible as n increases, so only the sum of the first 10 terms are shown in the solution depicted in Figure 2. Figure 2 shows solutions for dimensionless parameters for pressure $2\kappa p/Al^2$ and length x/l such that the layer length scale and pore pressure excess vary between 0 and 1.

The steady state solution can be determined by evaluating equation (3) at $t = \infty$

$$p_{(x)}\Big|_{t=\infty} = A\left(\frac{l^2 - x^2}{2\kappa}\right) \tag{4}$$

and the maximum pore pressure that results in the layer is that directly in the center at $x = 0$. The resulting expression for this maximum pressure is

$$p_{(0)}\Big|_{t=\infty} = A\left(\frac{l^2}{2\kappa}\right). \tag{5}$$

This expression can be plotted graphically to highlight the conditions under which pore fluid excess pressure can develop within a fault gouge layer.

Figure 3 shows how the magnitude of steady state overpressure development varies as a function of pore pressure production rate A and a characteristic time l^2/κ that includes the layer thickness and the hydraulic diffusivity of the gouge. This characteristic time can be used to estimate the time required for steady state behavior to establish. Ikari et al. (2009) (their equation 9) and Morrow et al. (2017) used this characteristic time to infer that the influence pore fluid pressure might have had on the measurements made of the friction coefficient of low-permeability gouges. (Note that Morrow et al., 2017, define l as the whole layer thickness so that the half layer thickness is $l/2$; hence, their characteristic time is $l^2/4\kappa$). The relations developed in Walder and Nur (1984) to analyze larger scale crustal fluid flow could also be used to similar effect. In the

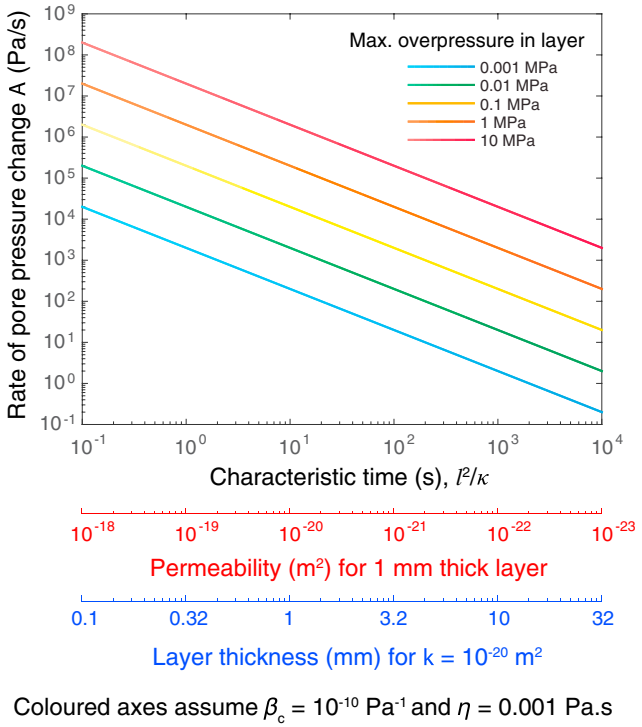

Figure 3. An illustration of the steady state excess pore fluid pressures that develop in the center of a gouge layer as a function of a characteristic time, permeability, or layer thickness, given a constant rate of pore fluid pressure production *A*.

analysis here, the typical values for sample storage capacity β_c and fluid viscosity η were chosen (Faulkner & Rutter, 2000; Wibberley, 2002) in order to allow the maximum overpressure to be presented as a function of compaction rate and (a) permeability (assuming constant layer thickness) and (b) layer thickness (assuming constant permeability). Permeability values from 10^{-18} m^2 to 10^{-23} m^2 are represented, which broadly covers the range of fault core materials (Faulkner et al., 2010). For fault gouge thickness, values vary from 0.1 mm to 32 mm. This range covers fault gouge layer thicknesses used in laboratory experiments but stops short of fault gouge thicknesses that can develop in nature, with some faults developing a fault core of several meters thickness (Faulkner et al., 2008). It may be seen that the lowest values for permeability and largest gouge layer thicknesses strongly favor the development of pore fluid overpressure.

Equation (5), or the graph presented in Figure 3, could be used by experimentalists to plan appropriate experimental configurations and conditions. In particular, the sliding velocity imposed in experiments must be sufficiently slow to ensure that significant internal pore fluid overpressures do not develop, resulting in low apparent friction coefficients. However, to employ the solutions presented, some prior knowledge of gouge layer permeability must be known, in addition to the compaction rate of the gouge as a function of slip rate. Morrow et al. (2017) use the experimental data for typical hydraulic diffusivities of clay-rich gouge produced by Wibberley (2002) to estimate the characteristic pressure decay times. Unfortunately, data characterizing compaction rates are not readily available.

The analytical solution is not able to reproduce the strength evolution with slip, because during an experiment several of the parameters such as the permeability k and storage capacity β_c will vary as a function of the compaction (i.e., porosity). Furthermore, fluid viscosity, η, and fluid compressibility change as a function of the fluid pressure. This makes the problem nonlinear and necessitates a numerical approach. Some of these data, and how they vary with slip, are not readily known but the relevant parameters can be determined from friction experiments and used to predict pore fluid pressure in gouge layers as is outlined in the next section.

3. Experimental Methodology and Materials

In order to determine the effect pore fluid pressure development within a fault gouge layer has on the bulk friction coefficient (μ, defined as shear stress divided by normal stress minus the imposed pore fluid pressure at the boundaries of the layer), a series of confined direct-shear friction experiments were performed at varying slip rates. An additional experiment was performed to determine the input parameters, and how they change during shear, for incorporation into the numerical modeling.

Confined, frictional sliding experiments were performed using low-permeability smectitic gouge derived from the principal slip zone of the Alpine Fault, recovered as part of the first phase of the Deep Fault Drilling Project (DFDP-1) (Sutherland et al., 2012). The gouge was recovered from 128.42 m depth in DFDP1B borehole and is similar to what was described as "brown gouge" by Boulton et al. (2014). The mineralogy of the gouge is as follows: quartz (28%), K feldspar (7%), plagioclase (20%), calcite (5%), muscovite/illite (13%), smectite (montmorillonite) (22%), chlorite (clinochlore) (4%), and rare analcime. The gouge was disaggregated and put through a sieve to ensure that all particles were less than 125 μm.

The friction experiments were performed using a servo-controlled triaxial deformation apparatus designed and built in Liverpool. The triaxial deformation apparatus can produce and control confining pressures up to 250 MPa (controlled to ±0.01 MPa) and pore pressures up to 200 MPa (controlled to ±0.01 MPa). Measurements of differential axial load (300 kN maximum) are made via an internal force gauge with an accuracy better than 0.05 kN. Axial load is provided by an electromechanical ballscrew actuator that can be

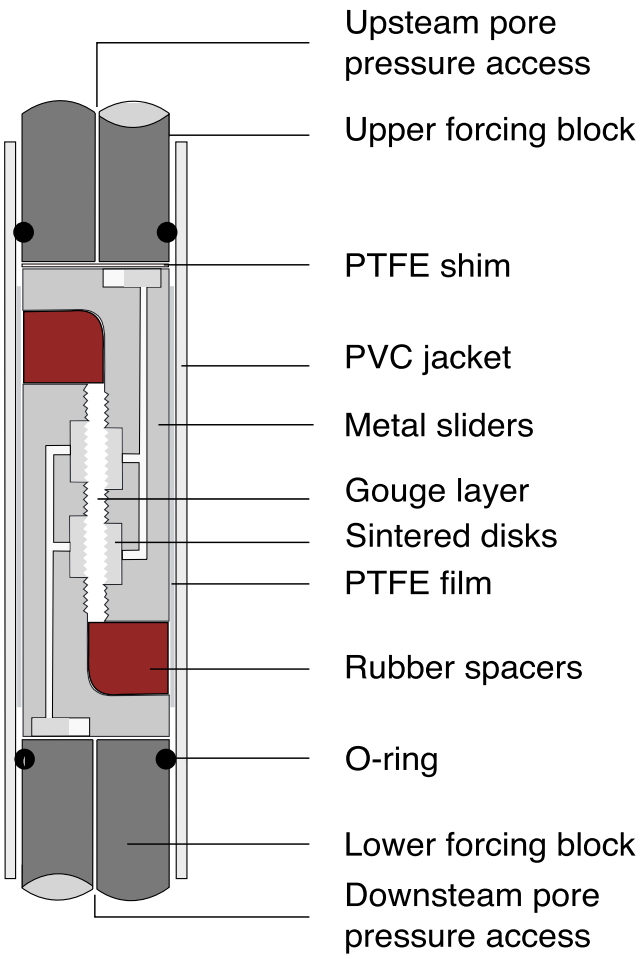

Figure 4. An illustration of the configuration of the sample assembly used in the experiments. The piston diameter is 20 mm. The arrangement was placed into a pressure vessel where the confining pressure provided the normal stress across the gouge layer. The pore fluid pressure was servo-controlled at the boundaries of the gouge layer through the porous stainless steel sintered disks.

controlled using a force or displacement feedback loop. A linear variable differential transformer attached to the piston of the pore pressure control pump provides detail of any pore volume change within the sample (volumometry) with a resolution better than 0.05 mm^3, while a constant pore fluid pressure setpoint is maintained. Further details of the deformation apparatus can be found in Faulkner and Armitage (2013).

A direct shear sample assembly was used in the experiments, where a layer of fault gouge was placed in between two steel forcing blocks (Figure 4). Pore pressure is supplied to the gouge layer via porous stainless steel frits that are push fitted into the sample sliders. The forcing block, where in contact with the gouge, has a series of 100 μm deep machined grooves to ensure coupling between gouge and forcing block. The fault gouge layer is designed so that it is oriented parallel to axial load, such that the layer is said to experience direct shear. The direct-shear configuration differs from more conventional triaxial friction tests where the gouge layer is applied to an inclined saw cut. In the inclined saw cut arrangement, confining pressure must be controlled to keep the normal stress on the layer constant; otherwise, it would increase with the application of load. Rapid control of the confining pressure is required during velocity stepping experiments, which is negated by using the direct-shear assembly. Another advantage of direct-shear experiments is that the strain hardening (i.e., increasing apparent frictional strength with displacement) sometimes seen in triaxial inclined saw cut experiments as a product of the sample geometry does not occur. The direct-shear configuration used was first developed for friction experiments by Logan et al. (1992) and modified more recently by the laboratories of Utrecht and Liverpool (Samuelson & Spiers, 2012; Sánchez-Roa et al., 2016).

Samples were prepared by weighing 1 g of gouge and leveling the room-dry powder onto one of the sliders in a jig. The layer was preloaded under ambient conditions to 5 MPa in a uniaxial press. The loading produced a compacted layer that was easier to load with the sliders into the PVC jacket used for confinement without sample loss. A PTFE shim with a central hole was placed on one side of the sample (see Figure 4) to allow one of the sliders to move laterally if compaction of the sample occurred. The samples were loaded into a sample assembly and placed into the triaxial deformation apparatus. In order to ensure experimental reproducibility, all samples underwent the same sequence of application of confining pressure and introduction of the water pore fluid. The confining pressure was increased to 60 MPa. Pore fluid was introduced (~1 MPa/s) into the sample up to 10 MPa. The sample was left for approximately 1 h to ensure it was fully saturated with pore fluid. The confining pressure and pore pressure were then increased to 70 MPa and 20 MPa, respectively, and left for 30 min. Small pressure transients were introduced across the sample to gain a qualitative measure of the time for equilibration. The confining pressure and pore pressure were then increased in 10 MPa increments with the same equilibration times until the test conditions of 100 MPa confining pressure and 40 MPa pore pressure were reached.

During the slowest slip rate tests (0.05 μm/s), the evolution of the permeability perpendicular to the layer was monitored continuously throughout the experiment. This was done by creating a small pore pressure oscillation (0.5 MPa peak-to-peak amplitude) on one side of the sample and observing the emergence of the oscillation through the sample into a small, fixed volume reservoir on the other side of the sample (Fischer & Paterson, 1992; Kranz et al., 1990). The permeability was determined from the ratio of the amplitudes and the phase shift of the pressure wave on either side of the sample. As long as the period of the pressure oscillation is small in comparison to any changes in permeability in the sample, the method provides useful

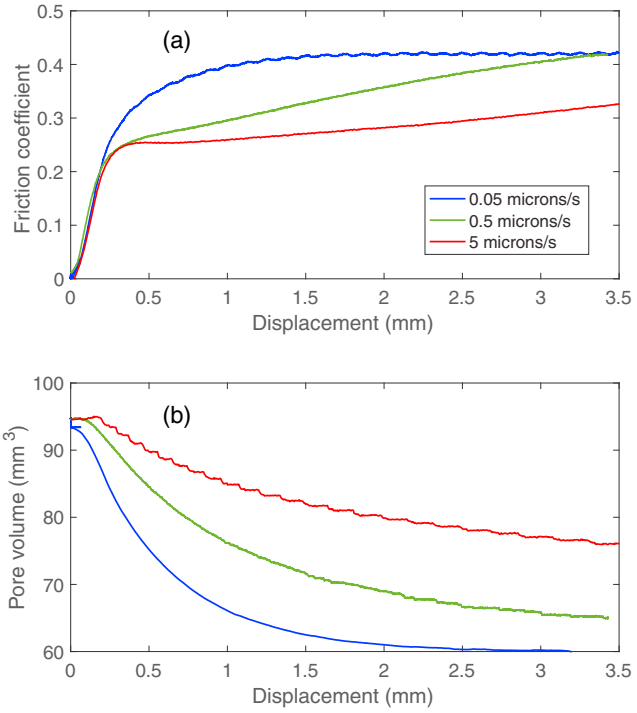

Figure 5. Experimental results showing (a) the change in the friction coefficient with slip displacement and (b) evolution of the pore volume with slip displacement (bottom) for different displacement rates. The normal stress applied was 100 MPa, and the pore pressure was controlled at the gouge layer boundaries at 40 MPa.

information on the evolution of permeability (Crawford et al., 2008; Fischer & Paterson, 1992). The sample storage capacity could not be determined reliably using this method due to the configuration of the pore volume system (see Bernabe et al., 2006).

4. Experimental Results

Experiments were performed at three sliding velocities: 0.05 μm/s, 0.5 μm/s, and 5 μm/s up to 3.5 mm of slip. Three sliding velocities were chosen to observe any difference in the mechanical response of that gouge due to the development of excess pore fluid pressure within the sample. Figure 5 shows the frictional strength (μ) and pore volume evolution of these tests as a function of slip. Results show a clear, systematic dependence of the friction coefficient and pore volume change on displacement rate. Faster slip rates result in yield at a lower friction coefficient, followed by strain hardening. The amount of pore compaction is also less at higher slip rates. All experiments were repeated at least once, with a high degree of data reproducibility.

Tests at the slowest displacement rate (0.05 μm/s), where the smallest pore fluid overpressures within the gouge layer are expected, were used as a baseline for the numerical modeling. Once slip had commenced, these tests lasted nearly 20 h. Permeability and pore volume evolution were measured, and the results from one of these tests are presented (Figure 6). The permeability reduces by ~1 order of magnitude during 3.5 mm slip, starting from just over 10^{-21} m^2. The starting pore volume of the samples could be determined by measuring the final thickness of the layer after the sample was removed from the sample assembly. The average was 0.74 mm. Some elastic unloading of the specimen is expected to have occurred following removal of the confining pressure, but this is expected to be insignificant and is ignored here. The total volume of 458.8 mm^3 can be compared with the solid volume of 1 g mass of the gouge used in the experiment (401.4 mm^3, with a density of 2.491 g/cm^3 measured by helium pycnometry) to find the final porosity which was determined to be 12.5%. The changes in the pore volume measured during the experiment can be used to back calculate the porosity evolution during the experiment (Figure 6). The starting porosity before shear commenced was calculated to be 19.1%, giving a starting layer thickness following hydrostatic compaction, but before shear, of 0.8 mm.

5. Fluid Pressure Buildup Due to Compaction During Loading and Shear in Low-Permeability Fault Gouges: Varying κ and A

The results shown in Figure 6 demonstrate that there are significant changes to the permeability and the pore volume during shear. The permeability will affect the hydraulic diffusivity κ, whereas the pore volume will affect the storage capacity (and thus κ) and also the pore pressure generation rate A. Consequently, equation (1) becomes nonlinear and the steady state analysis presented in section 2 cannot be used to assess pore fluid pressure development. Consequently, numerical modeling of equation (1) was undertaken to understand the development of pore fluid pressure during shear. The input parameters for the model were derived from the experimental measurements described above. The parameters required for numerical modeling, specifically hydraulic diffusivity and pore pressure production rate, and how they varied with time, were obtained from the experimental data as explained below.

5.1. Hydraulic Diffusivity κ

Hydraulic diffusivity (equation (2) and Figure 7) was determined from the measurements of permeability and the porosity (used to calculate the sample storage capacity, explained below), along with values for water compressibility and viscosity at 40 MPa obtained from the National Institute of Standards and Technology Chemistry WebBook (Linstrom & Mallard, 2017). The storage capacity depends on the (connected) porosity

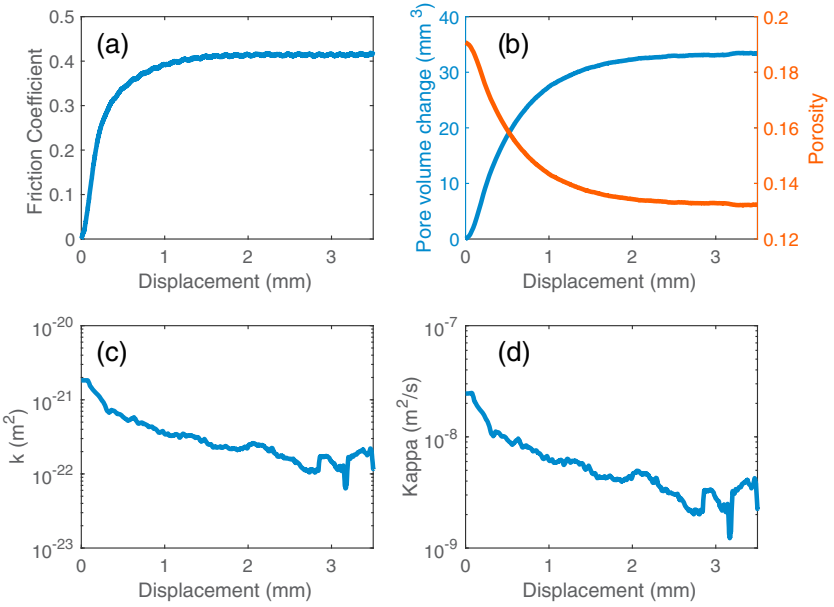

Figure 6. Results from the slowest displacement rate experiment (5 μm/s) where very limited development of pore fluid pressure was expected. From this, a baseline of parameters required for modeling could be established, including the evolution of (a) friction coefficient, (b) the change in pore volume, (c) the permeability, and (d) the hydraulic diffusivity, as a function of slip displacement.

ϕ, bulk compressibility of the sample β_b (Pa^{-1}), the fluid compressibility β_f (Pa^{-1}), and the compressibility of the constituent minerals β_m (Pa^{-1}) (Brace, Walsh, & Frangos, 1968; Faulkner, 1997)

$$\beta_c = \beta_b + \phi\beta_f - (1+\phi)\beta_m. \tag{6}$$

The bulk compressibility of crystalline rock is on the order of 20 times lower than water at the conditions of these experiments (Brace, 1965; Brace et al., 1968). The compressibility of constituent minerals is lower still. While the compressibility of fault gouge may be somewhat higher than that of crystalline rock, it is assumed here that the dominant term in equation (6) is porosity multiplied by the fluid compressibility. Hence, the storage capacity approximates as

$$\beta_c \approx \phi\beta_f. \tag{7}$$

Using the values for porosity in Figure 6 to calculate β_c ignores the effect of the confining pressure that will produce a volume reduction of the sample according to the bulk compressibility.

Once calculated, the overall development of hydraulic diffusivity with slip (δ) was fitted with the Hill-Langmuir equation (originally developed to describe the oxygen binding curve of hemoglobin and the adsorption of gases on surfaces; Hill, 1910; Langmuir, 1918):

$$\kappa = \kappa_0 - \frac{\kappa_{max}(\delta)^n}{(\delta_{0.5})^n + (\delta)^n}. \tag{8}$$

There is no physical significance for this, only that the equation produced a good fit to the data. The fit was done to smooth out some of the changes in the hydraulic diffusivity from the measurements of the permeability and porosity change. The very low permeability at the end of the experiments (Figure 6) is difficult to measure as it is subject to variation from small changes in conditions such as temperature fluctuations in the laboratory.

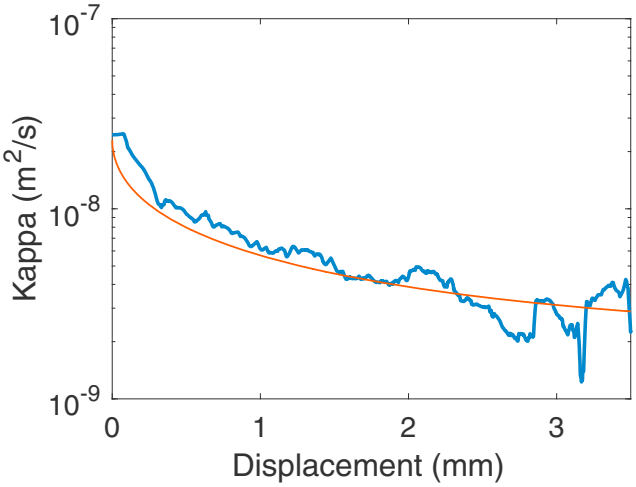

Figure 7. The variation in hydraulic diffusivity κ with displacement for the experiment at 0.05 μm/s, calculated using the measured permeability and pore volume change and published values for water viscosity. The fit to these data is also shown in red, which was used in the modeling.

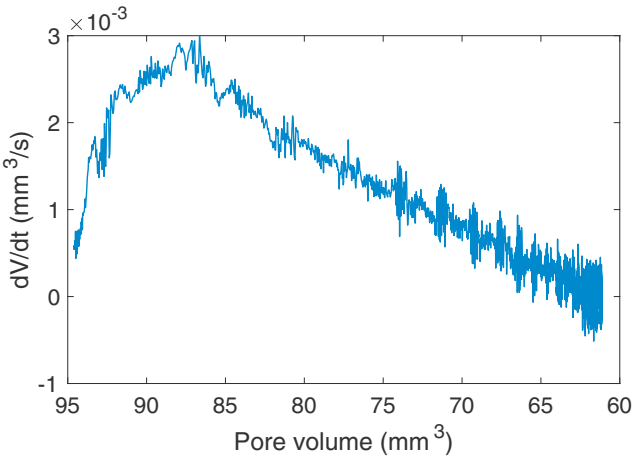

Figure 8. The rate of pore volume reduction measured using pore volumometry in the slowest experiment (0.05 μm/s) plotted as a function of the pore volume. This reduction in pore volume was used to calculate the increase in pore fluid pressure with each time step in the numerical model.

The changes of sample permeability and storage capacity with slip are accounted for in the numerical modeling using the fit above. However, these values for the hydraulic diffusivity do not account for suppressed compaction due to elevated pore fluid pressure, described in the next section and by equation (9). The porosity variation could be accounted for within the calculation of the storage capacity but the permeability will also depend on the porosity and this relationship is not known as it will also depend on the shear strain. To an extent, the decrease in permeability due to porosity loss will be offset by any decrease by the storage capacity. In order to base the analysis on the experimental measurements and to save any further assumptions on the relation between permeability, slip, and porosity, the hydraulic diffusivity described by equation (8) is used in all the calculations. Further, any variations in permeability and viscosity with distance across the gouge layer are not considered. Permeability and viscosity values depend on the fluid pressure that develops within the layer, but small variations in these numbers are not expected to affect the results of the analysis significantly.

5.2. Pore Pressure Production Rate *A*

The development of the pore pressure within the layer is due to the competing processes of pore pressure production through compaction and fluid loss from fluid flow to the drained boundaries. Initial modeling attempts in this work considered the compaction of porosity as a function of slip displacement. However, Figure 6 shows that pore compaction (i.e., porosity decrease) depends not only on slip but also on the slip rate, as differing volumes of pore fluid are expelled due to compaction as the displacement rate varies.

This result suggests that the amount of compaction depends on the pore fluid pressure that develops within the layers. As slip rate increases, higher internal pore fluid pressures reduce the effective normal stress, thus mediating further sample compaction. Consequently, less compaction occurs, less fluid volume is expelled, and more weakening is evident. In this case, the gouge will possess higher porosity at higher displacement rates further into the slip history; when displacement rates are lower, porosity is also lower as pore fluid pressures will dissipate and higher effective normal stress will drive compaction. A lower bound to the evolution of porosity with slip will be provided by the lowest slip displacement experiment where little or no excess pore fluid pressure develops.

In order to capture this aspect of the mechanical behavior, the compaction history was determined for each time step in the model by considering the compaction rate as a function of porosity and pore fluid pressure. The compaction rate in the 0.05 μm/s test, measured using pore volumometry, was plotted as a function of the pore volume (Figure 8) so an analytical expression for the compaction rate as a function of pore volume could be determined (a fifth-order polynomial was used). Using this relationship, the rate of compaction of the pore space ceases to be a function of the displacement, or the slip velocity. It only depends on the pore volume.

Then, the effect of the pore fluid pressure on compaction for each time step was taken into account by the second bracketed expression in the following equation:

$$\Delta\phi = f(\phi)\left(1 - \frac{p_{\text{excess}}}{p_{\text{eff}}}\right). \tag{9}$$

Here if no increase in p_{excess} ($= p - p_0$) develops through compaction, then the expression in the brackets is zero and the compaction rate is only a function of the pore volume according to the relationship in Figure 8. When the pore fluid pressure excess approaches the effective confining pressure p_{eff} at the boundaries (also the effective normal stress), the second term on the right-hand side tends to zero, and the compaction also tends to zero. Finally, the rate of change of porosity $\dot{\phi}$ is converted to a pore fluid pressure production rate by dividing by the compressibility of water

$$A = \dot{\phi}/\beta_f. \tag{10}$$

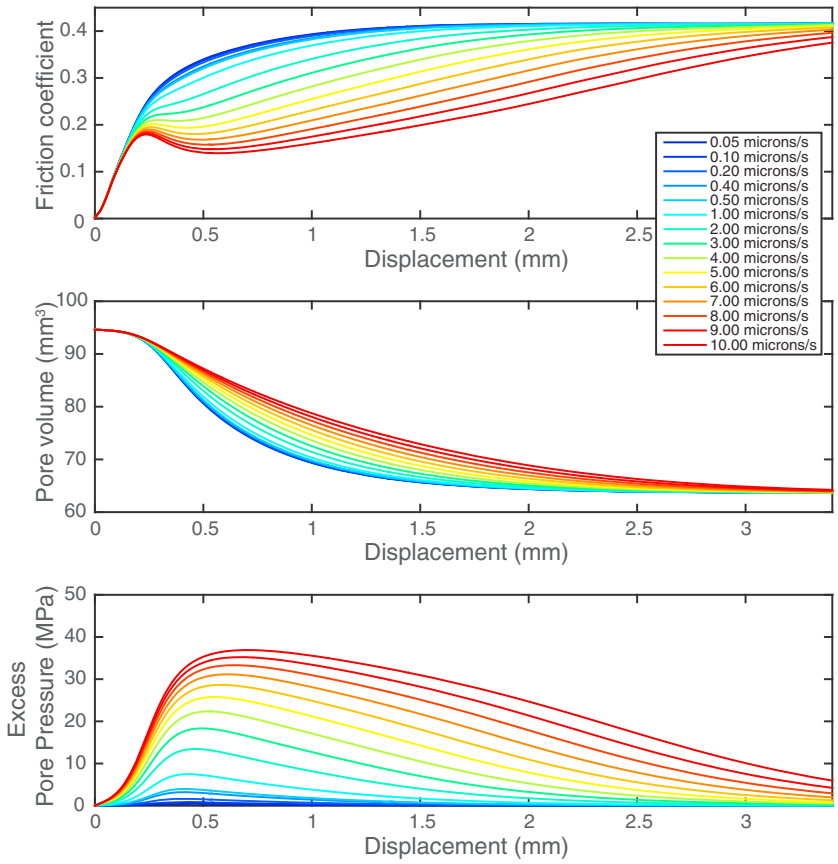

Figure 9. Modeled changes in friction coefficient, pore volume, and excess pore fluid pressure ($p - p_0$) with displacement as a function of displacement rate. The properties used in the modeling were from experiments with a normal stress of 100 MPa, and a pore pressure of 40 MPa was used as a boundary condition at the margins of the gouge layer.

The analysis here is likely applicable to most fault gouges undergoing shear. However, the compaction rate as a function of pore volume must be known. While the relationship used in modeling is based on the experimental results shown in Figure 8, the form of this curve may be representative of many gouges, even if the magnitude is uncertain. Future experimental studies could focus on the quantification of this compaction behavior for gouges containing varying amounts of clay in order to gain a more general understanding of this process.

5.3. Numerical Results

The development of excess pore fluid pressure within the gouge layer was modeled using an implicit Crank-Nicolson scheme (Recktenwald, 2011) that considers changes in the hydraulic diffusivity and pore pressure production rate with each time step. The layer is divided into 20 divisions and the pressure calculated within each of these for every time step. The resultant frictional strength was calculated using

$$\mu = \frac{\tau}{(\sigma_n - p)} \tag{11}$$

where the "real" shear stress τ is that required to shear the layer in the absence of any pore fluid pressure excess was determined from the experiments run at 0.05 μm/s, using the measured values for μ and modeled values for p. These values for τ were then used to calculate μ for all the other slip velocities. The values for p were obtained from averaging the central 10 values for the pore pressure within the layer rather than taking the maximum value for p which would imply that the deformation would localize in the center of the layer, which is generally not seen in microstructural analyses of clay-rich fault gouges.

Figure 9 shows the results from the numerical experiments. In form, they compare well with the results from experiments shown in Figure 5, suggesting that the approach used captures most aspects of the underlying physics. However, other factors cannot be excluded that may be important in causing slip hardening

behavior, such as grain size reduction and associated porosity changes. The aim of the numerical modeling was not to reproduce perfectly the experimental data but rather to reproduce the general experimental behavior using the fewest parameters possible. While additional complexity could be introduced into the model, this would necessitate further assumptions.

Figure 9 also serves to illustrate that for a "typical" shear experiment with a low-permeability fault gouge, displacement rates above ~0.4 μm/s will produce mechanical results that are compromised by pore fluid pressure development within the layer. Extrapolating from this result, for a gouge that has 1 order of magnitude higher permeability, displacement rates of ~4 μm/s might be acceptable. It is clear, however, that typical compaction rates for a range of gouges would be useful for experimentalists in order to constrain displacement rates above which significant pore fluid pressures will develop.

6. Effects of Pore Pressure Transients on Rate and State Friction Parameters

Experimentalists understand qualitatively that compaction-induced pore pressure transients affect the bulk strength of the sample and often design experiments to avoid them (Morrow et al., 2017). However, the effects of pore pressure transients on the rate and state frictional properties of fault gouges are more subtle and may provide misleading experimental results.

Here the effect of pore pressure transients on the mechanical behavior of experimental gouge samples subjected to rate (or velocity) steps is analyzed numerically. First, the development of pore pressure is predicted during a "run-in" period at a relatively slow displacement rate (0.0375 μm/s) up to 1.5 mm slip. The frictional strength of this run-in period is based on the shear stress from the 0.05 μm/s test that is largely unaffected by any pore pressure development owing to the slow displacement rate and long duration of the test. The evolution of the friction coefficient is then modeled using the rate and state formulation

$$\tau = (\sigma_n - p)\left[\mu_0 + a\ln\frac{V}{V_0} + b\ln\frac{V\theta}{D_c}\right] \tag{12}$$

where μ_0 is the initial steady state friction coefficient at slip velocity V_0 (m/s) before stepping to a new slip velocity V (m/s), a and b describe the magnitude of the direct effect and the state evolution, D_c (m) is the critical slip distance, and θ is the state parameter with units of time. The aging law is used to describe the state evolution (Ruina, 1983)

$$\frac{d\theta}{dt} = 1 - \frac{V\theta}{D_c}. \tag{13}$$

Equations (12) and (13) are coupled with the system stiffness described by

$$K(V - V_0) = \dot{\tau^e} \tag{14}$$

where K is the stiffness in Pa/m and τ^e is the elastic shear stress. While the gouge is actively yielding, the elastic shear stress will equal the shear stress in equation (12).

The results of this modeled response, in terms of the pore volume, pore fluid pressure, and strength evolution, are shown in Figure 10. Previous work by Boulton et al. (2014) determined the frictional parameters for this gouge to be approximately a = 0.01, b = 0.004, and D_c = 10 μm. The friction rate parameter ($a - b$) is positive; hence, the gouge is velocity strengthening. The stiffness K of our apparatus at these effective normal stresses during velocity steps is ~1,500 m^{-1} (strength in units of friction rather than Pascals). In general, owing to the slow run-in period, the buildup of pore fluid pressure is not large. However, there is still sufficient porosity to allow compaction at different rates during the velocity steps used to determine the rate and state friction parameters. This results in pore fluid pressure changes that significantly affect the rate and state friction parameters (Figure 11).

While constant values for a, b, and D_c have been used, the development of the pore fluid pressure makes it appear that the first two velocity steps produce velocity-weakening behavior (negative $a - b$). Figure 11 shows as text the results of inversion for a, b, D_c and K using non-linear least squares routine described by Noda and Shimamoto (2009). Pore fluid pressure transients become low enough for the intrinsic frictional behavior to become evident at displacements of greater than 2.5 mm (Figures 10 and 11). Testing the numerical results here with experiments was planned but, owing to the limited availability of the DFDP gouge,

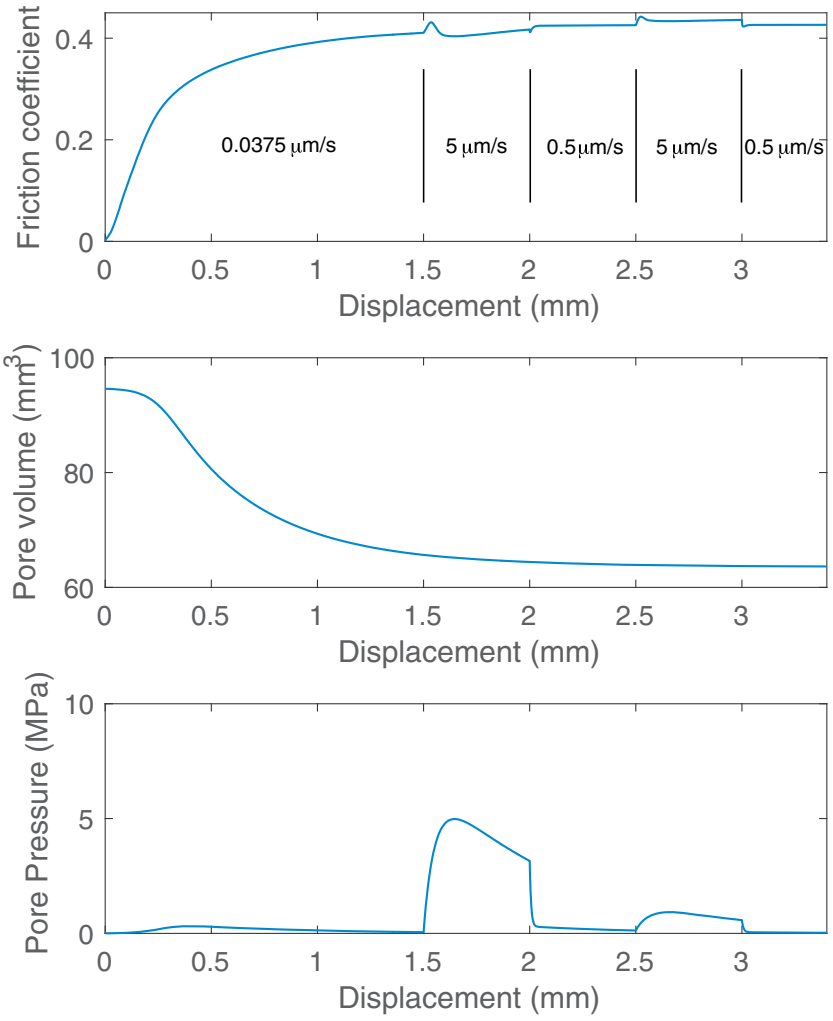

Figure 10. Modeled experimental response of a velocity stepping experiment. The displacement rates for each of the steps are shown, and the intrinsic rate and state response ($a = 0.01$, $b = 0.004$, $D_c = 10$ μm, and $K = 1500$ m^{-1} (units of friction)) is coupled with the influence of pore fluid pressure development.

insufficient material was available for experiments. In the velocity-stepping experiments performed by Boulton et al. (2014) the run-in velocity was 0.01 μm/s, compared to 0.0375 μm/s in the model. A velocity step at 1.4 mm displacement showed velocity neutral behavior, consistent with the modeling results.

The modeling here ignores any dilatant effects, that is, an increase in gouge layer thickness, that may occur during velocity steps (Lockner & Byerlee, 1994; Samuelson et al., 2009) that might mediate the effects described. Ikari et al. (2009) reported dilatant behavior during increases in velocity in clay-rich materials. Ikari et al. (2009) saw *only* dilational effects and did not report any compaction during their experiments. However, total slip was much larger in their experiments (up to 10–20 mm slip on a 2 mm thick gouge layer, equivalent to shear strains of 5–10). Thus, it is likely that at higher shear strains, experimental gouges reach a steady state porosity less susceptible to fluid-pressure transients. At lower shear strains, such as those reached in our experiments, dilatancy during velocity up-steps may cause a pore fluid pressure response that acts in the opposite way on the pore fluid pressure to the compaction effect discussed above; that is, increasing porosity due to dilation can decrease pore fluid pressure, thereby increasing the value of a (see also Samuelson et al., 2009).

Pore fluid pressure effects may also influence attempts to measure frictional or "Dieterich" strengthening that occurs during cessation of slip during slide-hold-slide experiments (Dieterich & Kilgore, 1994). If excess pore fluid pressures are present within the layer, then they will dissipate when the experiment is held stationary, giving the impression that the gouge strengthens during the hold period. This strengthening may be

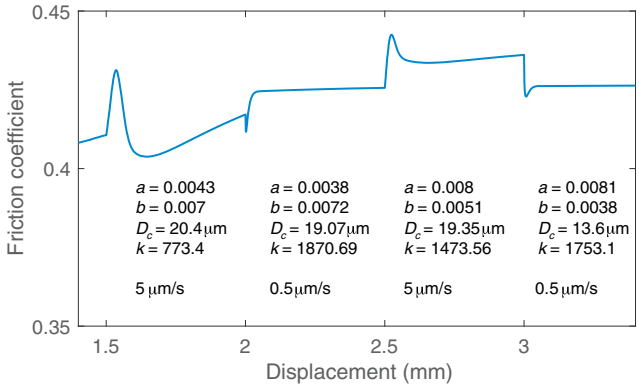

Figure 11. Detail of the modeled velocity steps shown in Figure 9. All steps were modeled using the same intrinsic rate and state friction parameters ($a = 0.01$, $b = 0.004$, $D_C = 10$ μm, and $K = 1500$ m^{-1} (units of friction)). The fitted parameters of the system response including pore fluid pressure effects are shown on the figure. The pore fluid pressure produces an apparent velocity weakening response for the first two velocity steps and only shows similar rate and state parameters to the intrinsic values in the final two steps. The properties used in the modeling were from experiments with a normal stress of 100 MPa, and a pore pressure of 40 MPa was used as a boundary condition at the margins of the gouge layer.

misinterpreted as a material property. Furthermore, successive, longer hold periods could yield results that show a positive correlation of strengthening with hold time. The analysis presented in this paper suggests that for gouge layers that are internally partially drained or undrained, longer hold times would show more apparent frictional strengthening as they give more time for excess pore fluid pressure within the layer to equilibrate with the layer boundaries. One way to determine whether this diffusion of pore fluid overpressures has influenced experimental slide-hold-slide results would be to repeat the hold times in reverse order (i.e., decreasing the hold time with successive slip intervals) to check if the same strengthening behavior is observed.

7. Implications for Natural Faulting

The experiments and analyses above suggest that yielding of natural low-permeability fault gouges can occur at lower shear stress than is suggested by their intrinsic frictional properties (Figure 9). During continued slip, when compaction rates are significant, the gouge could display apparent slip weakening due to the development of pore fluid pressure (e.g., Ito et al., 2017). Consequently, velocity weakening could occur within velocity strengthening materials as an artifact of pore fluid overpressures at slow slip rates.

As slip continues, the capacity for shear-enhanced compaction diminishes. The results of Ikari et al. (2009) and Crawford et al. (2008) indicate that at low slip rates of μm/s, and shear strains of ~10, clay-bearing fault gouges are more or less fully compacted. Consequently, an obvious question to ask is "under what natural conditions do the effects of pore fluid pressure transients significantly influence the mechanics of fault zones?"

In normally consolidated or underconsolidated conditions, there is significant scope for pore pressures to develop during initial fault slip. Moreover, underconsolidated conditions are typically associated with low-permeability materials, such as those found in accretionary fore-arc regions (Bolton et al., 1998; Screaton et al., 1990). Here the compaction of sediments is limited by the development of high pore fluid pressures, leading to underconsolidated conditions. Fault development and growth in these environments could be strongly affected by the processes described in this work, with the development of overpressure during initial slip leading to nucleation of slip events, and also to the propagation of earthquake ruptures (e.g., Brantut & Rice, 2011). Splay faults that run into unfaulted, and therefore uncompacted sediments (by shear-enhanced compaction), could propagate more readily with the transient development of excess pore fluid pressures.

On mature faults, where slip would presumably have fully compacted fault gouges, there appears to be little scope for generating pore fluid pressure, apart from thermal pressurization (Faulkner et al., 2011; Rice, 2006). Deeper parts of faults close to the brittle-viscous transition could generate pore fluid pressure through viscous compaction following seismicity that might generate fracture porosity due to the higher strain rates (Blanpied et al., 1992; Giger et al., 2007; Sleep & Blanpied, 1992). For shallower faulting, other processes, one of which is discussed below, might serve to generate porosity.

Observations of the Principal Slip Zones (PSZs) of mature faults commonly show evidence of cyclicity that suggest the PSZ porosity may evolve during the seismic cycle (e.g., Cowan et al., 2003). As an example, the Alpine Fault Zone (South Island, New Zealand) PSZ has potentially accommodated several hundred kilometers of slip within a zone approximately less than 0.5 m. Even in a single earthquake with a displacement thought typical for this fault (around 8 m horizontal displacement (Sutherland et al., 2007)), the shear strain will be ~20 and any feature that initially cut across the PSZ should form an angle of less than 4° to the boundary, assuming uniform strain across the layer.

The Alpine Fault Zone PSZ, as revealed by drilling from the first phase of the DFDP project (Sutherland et al., 2012), shows several generations of fault gouges within borehole DFDP-1A, recovered from 90.67 to 90.75 m depth (Figure 12a). In the PSZ, the most recent generation of gouge, containing montmorillonite, forms

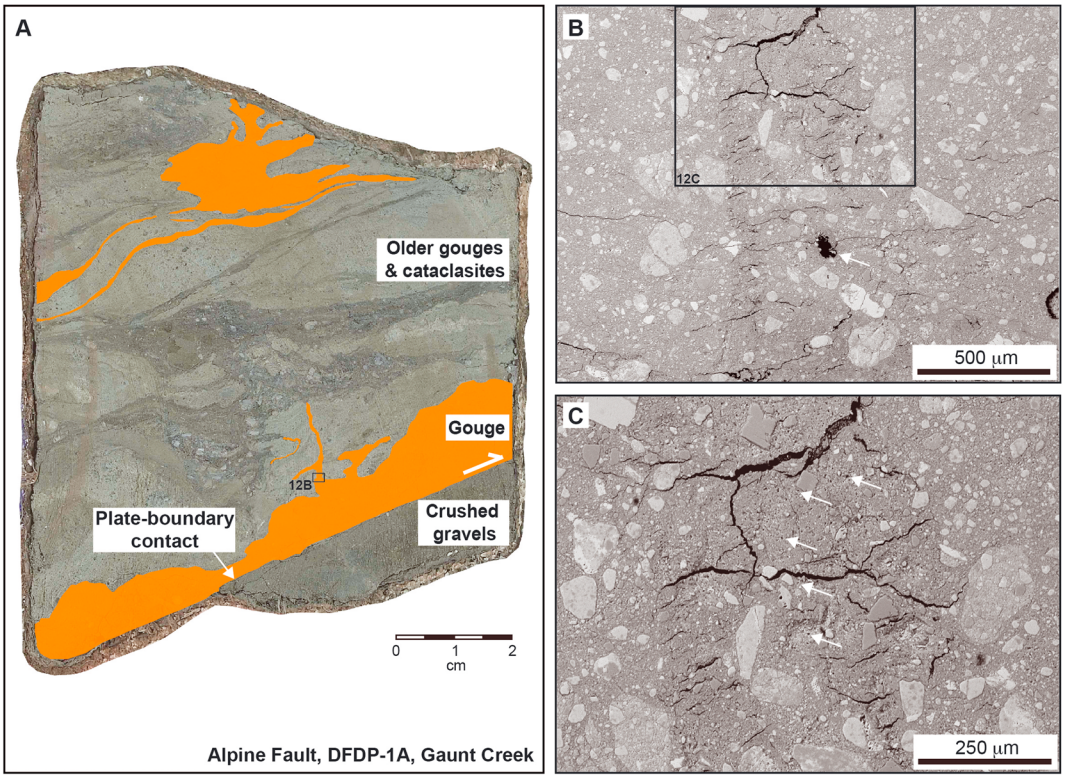

Figure 12. (a) Core of the Principal Slip Zone (PSZ) of the Alpine Fault in New Zealand recovered from ~90 m depth during the Deep Fault Drilling Project borehole DFDP-1A. In this figure, gouges containing montmorillonite are shaded in orange. The youngest gouges crosscut older blue-grey gouges and cataclasites containing chlorite/white mica. (b) Scanning electron microscope backscattered electron (SEM BSE) image enlargement of rectangular region outlined in *a*, the injection structure filled with gouge containing montmorillonite. The open cracks result from desiccation during thin-section preparation, and a thin section hole is indicated by the arrow. (c) SEM BSE image of the gouge within the injection structure. Note the abundant small open black holes, interpreted to be indicative of enhanced porosity in the fluidized gouge (arrowed). Together, these images illustrate the idea that the gouge becomes mobilized during earthquakes, shown by the crosscutting relationships and injection veins which would otherwise be sheared into an orientation subparallel to the boundaries. This may lead to a resetting of the porosity of the gouge with successive seismic events.

injection features that crosscut previously formed gouges (Boulton et al., 2012, 2014, 2017). As shown in Figures 12b and 12c, the crosscutting gouges with the lowest temperature clay minerals also exhibit lower porosity than the surrounding, older, gouges, which contain illite/muscovite and chlorite. The successive generation of fault gouge within the PSZ core implies that repeated slip occurred within this interval of brittle fault rocks.

One interpretation of the gouge structures presented in Figure 12 is that earthquakes on mature faults lead to a resetting of the structure of PSZs and their porosity by fluidization, possibly due to thermal pressurization. In this scenario, thermal pressurization results in low effective normal stress and gouge fluidization during which porosity is created; the fluidized gouge can then remain in an underconsolidated state if the effects of postseismic or interseismic creep are minor. Consequently, there is significant potential for creating conditions favorable for cyclical shear-enhanced compaction on seismogenic faults.

The results of the work presented have been directed toward understanding the compaction of clay gouges at low temperatures. However, the physical processes described are applicable to other regions of faults zones where compaction occurs but via different mechanisms. One such region is in the deeper regions of fault zones where elevated temperatures promote viscous deformation mechanisms (Giger et al., 2007; Sleep & Blanpied, 1992). The combination of brittle and viscous deformation, as well as the development of pore fluid pressure, could lead to complex deformation behavior in the deeper reaches of fault zones. Moreover, viscous compaction processes will occur under hydrostatic conditions and would not require shear stress in order to initiate.

8. Conclusions

In this work, the development of pore fluid pressure is considered analytically and also numerically. Constraints for the numerical modeling are derived from experiments on a natural low-permeability fault gouge. The model describes the behavior seen in experiments to a reasonable degree of accuracy, suggesting that the correct physical processes that occur have been captured by the modeling. The scope for producing pore pressure transients through shear-enhanced compaction during slip in low-permeability materials is considerable. These effects may significantly influence the results of laboratory measurements, in terms of bulk frictional strength and, more subtly, the determination of rate and state frictional properties. In nature, compaction leading to pore fluid overpressure generation could promote slip in natural environments in normally consolidated or underconsolidated fault zone materials. Gouge underconsolidation may be produced during seismic events where slip is accommodated at very low effective normal stresses due to thermal pressurization (e.g., Boulton et al., 2017; Brantut et al., 2010; Chen et al., 2013; Faulkner et al., 2011). In such a way, coseismic slip can prime principal slip zones for reshear by creating a microstructural state conducive to shear-enhanced compaction during the initial increments of fault slip.

Acknowledgments

D.R.F. gratefully acknowledges NERC grants NE/H012486/1, NE/J024449/1, and NE/P002943/1 and a Royal Society/Leverhulme Trust Senior Research Fellowship that helped support this work. C.S.R. acknowledges Research Training Grant BES-2012-052 562 from the Spanish Government. S.d. H. acknowledges a Marie Curie Fellowship. Discussions with Harsha Bhat during an early stage of this work helped with the development of the model. Gary Coughlan is thanked for technical assistance with the development and maintenance of the experimental apparatus. We thank reviewers David Lockner and Stephen Cox for their helpful comments that improved the manuscript. The data used are listed in the references and figures and are available on request from the corresponding author.

References

Behnsen, J., & Faulkner, D. R. (2011). Water and argon permeability of phyllosilicate powders under medium to high pressure. *Journal of Geophysical Research*, *116*, B12203. https://doi.org/10.1029/2011JB008600

Bernabe, Y., Mok, U., & Evans, B. (2006). A note on the oscillating flow method for measuring rock permeability. *International Journal of Rock Mechanics and Mining Sciences*, *43*, 311–316. https://doi.org/10.1016/j.ijrmms.2005.04.013

Bizzarri, A., & Cocco, M. (2006). A thermal pressurization model for the spontaneous dynamic rupture propagation on a three-dimensional fault: 1. Methodological approach. *Journal of Geophysical Research*, *111*, B05303. https://doi.org/10.1029/2005JB003862

Blanpied, M. L., Lockner, D. A., & Byerlee, J. D. (1992). An earthquake mechanism based on rapid sealing of faults. *Nature*, *358*(6387), 574–576. https://doi.org/10.1038/358574a0

Bolton, A. J., Maltman, A. J., & Clennell, M. B. (1998). The importance of overpressure timing and permeability evolution in fine-grained sediments undergoing shear. *Journal of Structural Geology*, *20*(8), 1013–1022. https://doi.org/10.1016/S0191-8141(98)00030-3

Boulton, C., Carpenter, B. M., Toy, V., & Marone, C. (2012). Physical properties of surface outcrop cataclastic fault rocks, Alpine Fault, New Zealand. *Geochemistry, Geophysics, Geosystems*, *13*, Q01018. https://doi.org/10.1029/2011GC003872

Boulton, C., Moore, D. E., Lockner, D. A., Toy, V. G., Townend, J., & Sutherland, R. (2014). Frictional properties of exhumed fault gouges in DFDP-1 cores, Alpine Fault, New Zealand. *Geophysical Research Letters*, *41*, 356–362. https://doi.org/10.1002/2013GL058236

Boulton, C., Yao, L., Faulkner, D. R., Townend, J., Toy, V. G., Sutherland, R., … Shimamoto, T. (2017). High-velocity frictional properties of Alpine Fault rocks: Mechanical data, microstructural analysis, and implications for rupture propagation. *Journal of Structural Geology*, *97*, 71–92. https://doi.org/10.1016/j.jsg.2017.02.003

Brace, W. F. (1965). Some new measurements of linear compressibility of rocks. *Journal of Geophysical Research*, *70*, 391–398. https://doi.org/10.1029/JZ070i002p00391

Brace, W. F., Walsh, J. B., & Frangos, W. T. (1968). Permeability of granite under high pressure. *Journal of Geophysical Research*, *73*, 2225–2236. https://doi.org/10.1029/JB073i006p02225

Brantut, N., & Rice, J. R. (2011). How pore fluid pressurization influences crack tip processes during dynamic rupture. *Geophysical Research Letters*, *38*, L24314. https://doi.org/10.1029/2011GL050044

Brantut, N., Schubnel, A., Corvisier, J., & Sarout, J. (2010). Thermochemical pressurization of faults during coseismic slip. *Journal of Geophysical Research*, *115*, B05314. https://doi.org/10.1029/2009JB006533

Byerlee, J. (1990). Friction, overpressure and fault normal compression. *Geophysical Research Letters*, *17*, 2109–2112. https://doi.org/10.1029/GL017i012p02109

Carslaw, H. S., & Jaeger, J. C. (1959). *Conduction of heat in solids* (2nd ed.). Oxford: Oxford University Press.

Chen, J., Yang, X., Duan, Q., Shimamoto, T., & Spiers, C. J. (2013). Importance of thermochemical pressurization in the dynamic weakening of the Longmenshan Fault during the 2008 Wenchuan earthquake: Inferences from experiments and modeling. *Journal of Geophysical Research: Solid Earth*, *118*, 4145–4169. https://doi.org/10.1002/jgrb.50260

Chester, F. M., Evans, J. P., & Biegel, R. L. (1993). Internal structure and weakening mechanisms of the San-Andreas Fault. *Journal of Geophysical Research*, *98*, 771–786. https://doi.org/10.1029/92JB01866

Chester, F. M., & Logan, J. M. (1986). Implications for mechanical-properties of brittle faults from observations of the punchbowl fault zone, California. *Pure and Applied Geophysics*, *124*(1-2), 79–106. https://doi.org/10.1007/BF00875720

Collettini, C., & Sibson, R. H. (2001). Normal faults, normal friction? *Geology*, *29*(10), 927–930. https://doi.org/10.1130/0091-7613(2001)029%3C0927:NFNF%3E2.0.CO;2

Cowan, D. S., Cladouhos, T. T., & Morgan, J. K. (2003). Structural geology and kinematic history of rocks formed along low-angle normal faults, Death Valley, California. *Geological Society of America Bulletin*, *115*(10), 1230–1248. https://doi.org/10.1130/B25245.1

Crawford, B. R., Faulkner, D. R., & Rutter, E. H. (2008). Strength, porosity, and permeability development during hydrostatic and shear loading of synthetic quartz-clay fault gouge. *Journal of Geophysical Research*, *113*, B03207. https://doi.org/10.1029/2006JB004634

Dieterich, J. H. (1979). Modeling of rock friction: 1. Experimental results and constitutive equations. *Journal of Geophysical Research*, *84*, 2161–2168. https://doi.org/10.1029/JB084iB05p02161

Dieterich, J. H., & Kilgore, B. D. (1994). Direct observation of frictional contacts - new insights for state-dependent properties. *Pure and Applied Geophysics*, *143*(1-3), 283–302. https://doi.org/10.1007/BF00874332

Faulkner, D. R. (1997). The role of clay-bearing fault gouges in controlling fluid pressures in fault zones: Implications for fault mechanics. (PhD thesis), (pp. 279). University Manchester, UK.

Faulkner, D. R., & Armitage, P. J. (2013). The effect of tectonic environment on permeability development around faults and in the brittle crust. *Earth and Planetary Science Letters*, *375*, 71–77. https://doi.org/10.1016/j.epsl.2013.05.006

Faulkner, D. R., Jackson, C. A. L., Lunn, R. J., Schlische, R. W., Shipton, Z. K., Wibberley, C. A. J., & Withjack, M. O. (2010). A review of recent developments concerning the structure, mechanics and fluid flow properties of fault zones. *Journal of Structural Geology*, *32*(11), 1557–1575. https://doi.org/10.1016/j.jsg.2010.06.009

Faulkner, D. R., Mitchell, T. M., Behnsen, J., Hirose, T., & Shimamoto, T. (2011). Stuck in the mud? Earthquake nucleation and propagation through accretionary forearcs. *Geophysical Research Letters*, *38*, L18303. https://doi.org/10.1029/2011GL048552

Faulkner, D. R., Mitchell, T. M., Rutter, E. H., & Cembrano, J. (2008). On the structure and mechanical properties of large strike-slip faults. In C. A. J. Wibberley, et al. (Eds). *The internal structure of fault zones—Implications for mechanical and fluid flow properties*, *Geological Society of London, Special Publications* (Vol. 299, pp. 139–150). https://doi.org/10.1144/SP299.9

Faulkner, D. R., & Rutter, E. H. (1998). The gas permeability of clay-bearing fault gouge at 20°C. In G. Jones, Q. Fisher, & R. J. Knipe (Eds.), *Faults, fault sealing and fluid flow in hydrocarbon reservoirs*, *Geological Society London, Special Publications* (Vol. 147, pp. 147–156). https://doi.org/10.1144/GSL.SP.1998.147.01.10, 1.

Faulkner, D. R., & Rutter, E. H. (2000). Comparisons of water and argon permeability in natural clay-bearing fault gouge under high pressure at 20°C. *Journal of Geophysical Research*, *105*, 16,415–16,426. https://doi.org/10.1029/2000JB900134

Faulkner, D. R., & Rutter, E. H. (2001). Can the maintenance of overpressured fluids in large strike-slip fault zones explain their apparent weakness? *Geology*, *29*(6), 503–506. https://doi.org/10.1130/0091-7613(2001)029%3C0503:CTMOOF%3E2.0.CO;2

Fischer, G. J., & Paterson, M. S. (1992). Measurement of permeability and storage capacity in rocks during deformation at high temperature and pressure. In B. Evans & T.-F. Wong (Eds.), *Fault mechanics and transport properties of rocks* (pp. 214–252). London: Academic Press.

Frank, W. B., Shapiro, N. M., Husker, A. L., Kostoglodov, V., Bhat, H. S., & Campillo, M. (2015). Along-fault pore-pressure evolution during a slow-slip event in Guerrero, Mexico. *Earth and Planetary Science Letters*, *413*, 135–143. https://doi.org/10.1016/j.epsl.2014.12.051

Garagash, D. I. (2012). Seismic and aseismic slip pulses driven by thermal pressurization of pore fluid. *Journal of Geophysical Research*, *117*, B04314. https://doi.org/10.1029/2011JB008889

Giger, S. B., Tenthorey, E., Cox, S. F., & Gerald, J. D. F. (2007). Permeability evolution in quartz fault gouges under hydrothermal conditions. *Journal of Geophysical Research*, *112*, B07202. https://doi.org/10.1029/2006JB004828

Hill, A. V. (1910). The possible effects of the aggregation of the molecules of hæmoglobin on its dissociation curves. *The Journal of Physiology*, *40*(suppl), i–vii. https://doi.org/10.1113/jphysiol.1910.sp001386

Hubbert, M. K., & Rubey, W. W. (1959). Role of fluid pressure in mechanics of overthrust faulting 1. Mechanics of fluid filled porous solids and its application ot overthrust faulting. *Geological Society of America Bulletin*, *70*(2), 115–166.

Ikari, M. J., Saffer, D. M., & Marone, C. (2009). Frictional and hydrologic properties of clay-rich fault gouge. *Journal of Geophysical Research*, *114*, B05409. https://doi.org/10.1029/2008JB006089

Ito, Y., Ikari, M. J., Ujiie, K., & Kopf, A. J. (2017). Coseismic slip propagation on the Tohoku plate boundary fault facilitated by slip-dependent weakening during slow fault slip. *Geophysical Research Letters*, *44*, 8749–8756. https://doi.org/10.1002/2017GL074307

Kranz, R. L., Saltzman, J. S., & Blacic, J. D. (1990). Hydraulic diffusivity measurements on laboratory rock samples using an oscillating pore pressure method. *International Journal of Rock Mechanics and Mining Sciences*, *27*(5), 345–352. https://doi.org/10.1016/0148-9062(90)92709-N

Langmuir, I. (1918). The adsorption of gases on plane surfaces of glass, mica and platinum. *Journal of the American Chemical Society*, *40*(9), 1361–1403. https://doi.org/10.1021/ja02242a004

Linstrom, P. J., & Mallard, W. G. (Eds.) (2017). *NIST chemistry webbook*. Gaithersburg MD: National Institute of Standards and Technology. 20899

Lockner, D. A., & Byerlee, J. D. (1994). Dilatancy in hydraulically isolated faults and the suppression of instability. *Geophysical Research Letters*, *21*, 2353–2356. https://doi.org/10.1029/94GL02366

Logan, J. M., Dengo, C. A., Higgs, N. G., & Wang, Z. Z. (1992). Fabrics of experimental fault zones: Their development and relationship to mechanical behavior. In B. Evans, & T.-F. Wong (Eds.), *Fault mechanics and transport properties of rocks* (pp. 33–69). New York: Academic Press.

Marone, C., Raleigh, C. B., & Scholz, C. H. (1990). Frictional behavior and constitutive modeling of simulated fault gouge. *Journal of Geophysical Research*, *95*, 7007–7025. https://doi.org/10.1029/JB095iB05p07007

Mitchell, T. M., & Faulkner, D. R. (2008). Experimental measurements of permeability evolution during triaxial compression of initially intact crystalline rocks and implications for fluid flow in fault zones. *Journal of Geophysical Research*, *113*, B11412. https://doi.org/10.1029/2008JB005588

Mitchell, T. M., & Faulkner, D. R. (2012). Towards quantifying the matrix permeability of fault damage zones in low porosity rocks. *Earth and Planetary Science Letters*, *339-340*, 24–31. https://doi.org/10.1016/j.epsl.2012.05.014

Morrow, C., Shi, L. Q., & Byerlee, J. (1981). Permeability and strength of San Andreas fault gouge under high pressure. *Geophysical Research Letters*, *8*, 325–328. https://doi.org/10.1029/GL008i004p00325

Morrow, C. A., Moore, D. E., & Lockner, D. A. (2017). Frictional strength of wet and dry montmorillonite. *Journal of Geophysical Research: Solid Earth*, *122*, 3392–3409. https://doi.org/10.1002/2016JB013658

Noda, H., & Lapusta, N. (2010). Three-dimensional earthquake sequence simulations with evolving temperature and pore pressure due to shear heating: Effect of heterogeneous hydraulic diffusivity. *Journal of Geophysical Research*, *115*, B12314. https://doi.org/10.1029/2010JB007780

Noda, H., & Shimamoto, T. (2009). Constitutive properties of clayey fault gouge from the Hanaore fault zone, southwest Japan. *Journal of Geophysical Research*, *114*, B04409. https://doi.org/10.1029/2008JB005683

Recktenwald, G. W. (2011). Finite-difference approximations to the heat equation.

Rice, J. R. (2006). Heating and weakening of faults during earthquake slip. *Journal of Geophysical Research*, *111*, B05311. https://doi.org/10.1029/2005JB004006

Rubin, A. M. (2008). Episodic slow slip events and rate-and-state friction. *Journal of Geophysical Research*, *113*, B11414. https://doi.org/10.1029/2008JB005642

Ruina, A. (1983). Slip instability and state variable friction laws. *Journal of Geophysical Research*, *88*, 359–370.

Samuelson, J., Elsworth, D., & Marone, C. (2009). Shear-induced dilatancy of fluid-saturated faults: Experiment and theory. *Journal of Geophysical Research*, *114*, B12404. https://doi.org/10.1029/2008JB006273

Samuelson, J., & Spiers, C. J. (2012). Fault friction and slip stability not affected by Co2 storage: Evidence from short-term laboratory experiments on North Sea reservoir sandstones and caprocks. *International Journal of Greenhouse Gas Control*, *11*, S78–S90. https://doi.org/10.1016/j.ijggc.2012.09.018

Sánchez-Roa, C., Jiménez-Millán, J., Abad, I., Faulkner, D. R., Nieto, F., & García-Tortosa, F. J. (2016). Fibrous clay mineral authigenesis induced by fluid-rock interaction in the Galera fault zone (Betic Cordillera, SE Spain) and its influence on fault gouge frictional properties. *Applied Clay Science*, *134*, 275–288. https://doi.org/10.1016/j.clay.2016.06.023

Screaton, E. J., Wuthrich, D. R., & Dreiss, S. J. (1990). Permeabilities, fluid pressures, and flow rates in the Barbados ridge complex. *Journal of Geophysical Research*, *95*, 8997–9007. https://doi.org/10.1029/JB095iB06p08997

Segall, P., & Rice, J. R. (1995). Dilatancy, compaction, and slip instability of a fluid-infiltrated fault. *Journal of Geophysical Research*, *100*, 22,155–22,171. https://doi.org/10.1029/95JB02403

Sleep, N. H., & Blanpied, M. L. (1992). Creep, compaction and the weak rheology of major faults. *Nature*, *359*(6397), 687–692. https://doi.org/10.1038/359687a0

Sutherland, R., Eberhart-Phillips, D., Harris, R. A., Stern, T., Beavan, J., Ellis, S., … Stirling, M. (2007). Do great earthquakes occur on the Alpine Fault in central South Island, New Zealand? In D. Okaya, et al. (Eds.), *A continental plate boundary: Tectonics at South Island, New Zealand* (pp. 235–251). Washington, DC: American Geophysical Union. https://doi.org/10.1029/175GM12

Sutherland, R., Toy, V. G., Townend, J., Cox, S. C., Eccles, J. D., Faulkner, D. R., … Kopf, A. J. (2012). Drilling reveals fluid control on architecture and rupture of the Alpine fault, New Zealand. *Geology*, *40*(12), 1143–1146. https://doi.org/10.1130/g33614.1

Walder, J., & Nur, A. (1984). Porosity reduction and crustal pore pressure development. *Journal of Geophysical Research*, *89*, 11,539–11,548. https://doi.org/10.1029/JB089iB13p11539

Wibberley, C. A. J. (2002). Hydraulic diffusivity of fault gouge zones and implications for thermal pressurization during seismic slip. *Earth, Planets and Space*, *54*(11), 1153–1171. https://doi.org/10.1186/BF03353317

Wibberley, C. A. J., & Shimamoto, T. (2003). Internal structure and permeability of major strike-slip fault zones: The median tectonic line in Mie Prefecture, Southwest Japan. *Journal of Structural Geology*, *25*(1), 59–78. https://doi.org/10.1016/S0191-8141(02)00014-7